Research Article | Vol. 27, No. 9 | 29 Apr 2019 | OPTICS EXPRESS 12832
Optics EXPRESS

Tapered fiber-based intravascular photoacoustic endoscopy for high-resolution and deep-penetration imaging of lipid-rich plaque

LEI WANG,[1,2] PENG LEI,[1] XUE WEN,[1] PENGFEI ZHANG,[3,4,5] AND SIHUA YANG[1,2,6]

[1]*MOE Key Laboratory of Laser Life Science & Institute of Laser Life Science, South China Normal University, Guangzhou 510631, China*
[2]*College of Biophotonics, South China Normal University, Guangzhou 510631, China*
[3]*Department of Cardiology, Qilu Hospital of Shandong University, Jinan 250012, China*
[4]*Key Laboratory of Cardiovascular Remodeling and Function Research, Chinese Ministry of Education and Chinese National Health Commission, Shandong University, Jinan 250100, China*
[5]*pengf-zhang@163.com*
[6]*yangsh@scnu.edu.cn*

Abstract: High-resolution intravascular photoacoustic (IVPA) imaging can potentially improve the identification of atherosclerosis plaque. However, the absorption of water and the low coupled laser energy resulted in insufficient excitation energy provided by the single-mode fiber-based IVPA endoscope to achieve high-resolution and deep-penetration plaque imaging. In this paper, we developed a 1 mm diameter IVPA endoscope assembled with a Ø25-Ø9 μm tapered fiber. Owing to high coupling efficiency and the small output facula of tapered fiber, the IVPA endoscope has an optimal lateral resolution of 18 μm and a large imaging-depth covering from the intima to the peri-adventitial adipose, as confirmed by imaging results respectively. Furthermore, IVPA imaging in the blood has confirmed that the tapered fiber-based endoscope can display the distribution and the relative concentration of lipid in *ex vivo* plaque precisely. By the obtained histology-like images, IVPA imaging shows great potential for accurately imaging atherosclerosis plaque.

1. Introduction

Cardiovascular disease (CVD) is one of diseases with the highest mortality rates in the world [1]. Most CVD events are associated with atherosclerosis plaque, the lipid content and lipid distribution within the plaque affect the tendency of atherosclerotic plaque rupture [2]. And the results of studies on human aortic plaque samples showed a positive correlation between lipid concentration and plaque vulnerability [3]. Unfortunately, existing mainstream imaging techniques, such as intravascular optical coherence tomography (IVOCT) and intravascular ultrasound (IVUS) imaging, still have certain limitations in accurately imaging these characteristics for identifying atherosclerosis plaque [4,5].

Photoacoustic (PA) imaging is a rapidly evolving technology, which can provide molecular, anatomic, and functional information about biological tissue [6–19]. Intravascular photoacoustic (IVPA) imaging has the advantages of high-resolution of optical imaging (i.e. IVOCT) and deep-penetration of US imaging (i.e. IVUS). Meanwhile, since the optical absorption spectrum is a distinct signature of component, IVPA can specifically identify chemical component with extremely high sensitivity [20,21]. Therefore, IVPA imaging inherently possesses an excellent capability to identify the component within plaque and map the morphological distribution of lipid.

#361688 https://doi.org/10.1364/OE.27.012832
Journal © 2019 Received 13 Mar 2019; revised 11 Apr 2019; accepted 13 Apr 2019; published 22 Apr 2019

Optics EXPRESS

High-resolution and deep-penetration imaging results can afford more accurate diagnosis of atherosclerotic plaque components, for instance, calcification, intra-plaque hemorrhage, and quantification of plaque area and volume [22]. However, energy attenuation in water leads to the insufficient laser energy delivered by a single mode fiber for high resolution and deep lipids imaging. According to absorption spectrum, the absorption peak of lipid is 1725 nm in the range from 500 nm to 2000 nm [23–25]. According to the laser attenuation formula: $E = E_0 * exp(-a_0 \times x)$, where E_0 expresses as initial laser energy, and E indicates as the laser energy after the laser passes through a uniform medium with a thickness of x and an absorption coefficient of a_0 [26]. The energy reduces to 30% of the initial energy when the laser with a wavelength of 1725 nm is irradiated onto the lipid surface through water of 2 mm thickness (the optical absorption coefficient of water at 1725 nm is 0.588). Therefore, the IVPA system requires fiber to deliver more laser energy to excite PA signals from lipids. To deliver laser energy, many IVPA systems in the previous literatures employed a multi-mode fiber that owned the characteristic of high coupling efficiency and damage threshold [27,28]. Nevertheless, the multi-mode fiber with or without a mating lens would result in the low lateral resolution and excitation efficiency due to space constraints of the intravascular endoscopic probe for IVPA imaging.

In theory, the high coupling efficiency of the fiber requires the waist of the laser beam to be smaller than the core diameter of fiber and the numerical aperture (NA) of laser to be smaller than the NA of fiber [29]. According to the diffraction limit formula of the laser focus spot: $R = 0.61 \times \lambda / NA$, where R expresses as facula size, λ indicates as the wavelength of the optical [30]. Then, the diffraction limit of the focused laser R is calculated to be 8.77 μm for the IVPA system with a 1725nm emitted wavelength and a single-mode fiber (the NA of the single-mode fiber with core diameter of 9 μm is 0.12). The diffraction limit of the focused laser (8.77 μm) is very close to the core diameter of the single-mode fiber (9 μm), which means that the coupling system has a small displacement tolerance. Thus, the angular deviation and vibration of the coupling device will lead to low coupling stability and damage threshold for the single-mode fiber, owing to the extremely small displacement tolerance. On the other hand, the near-infrared laser light emitted by the optical parametric oscillator (OPO) typically have poor laser quality factor (M^2), which makes laser beam be difficult to be efficiently coupled into the small core fiber. For those problems, we use a Ø25-Ø9 μm tapered fiber to solve the problem of insufficient laser energy due to the low coupling stability and damage threshold of the single-mode fiber. Due to high coupling efficiency and small output facula of tapered fiber, the laser energy output from the tapered fiber is several times higher than that of the single-mode fiber, which ultimately makes the IVPA obtain the high-resolution and deep-penetration lipids imaging.

2. Methods and materials

Figure 1(a) shows a schematic of the IVPA/US imaging system based on Ø25-Ø9 μm tapered fiber. A laser source (NT200 Series Laser, Ekspla, Vilnius, Lithuania) in the system delivers pulsed lasers at high pulse repetition rates of 2.5 kHz and laser-pulses duration of approximately 8 ns. The output laser is spatially attenuated and reshaped, and focused into the input end of tapered fiber with core diameter of 25 μm by an objective lens (RMS4X, Thorlabs, New Jersey, USA). The output end of tapered fiber with core diameter of 9 μm is connected to stator end of an optical-electric rotary joint (customized, MOFLON, Shenzhen, China). Finally, the laser is transmitted to endoscopic probe by using a fiber with a core diameter of 9 μm connected to the rotor end of the optical-electric rotary. The 1 mm diameter endoscopic probe structure chart is shown in Fig. 1(b) The endoscopic probe integrates 0.5 mm-diameter C-lens (customized, Fuzhou Gongxin Photoelectric Technology Co., Ltd., Fujian, China), 55° reflector (customized, Nanyang Jingliang Photoelectric Co., Ltd., Henan, China) and US transducer (customized, Suzhou institute of biomedical engineering and technology, Chinese academy of sciences, Suzhou, China), the endoscopic probe is rotation

Optics EXPRESS

and pullback by a double-layer torsion coil (customized, Asahi Intecc, Aichi, Japan). Inside the endoscopic probe, the laser is focused by the 0.5 mm-diameter C-lens and reflected by the 55° reflector, and converges 2 mm above the US transducer to form a focus to excite the PA signal. The PA signals are detected by the miniature single-element US transducer with a dimension of 0.6 × 0.5 mm^2, a center frequency of 50 MHz, and a bandwidth of 80%, which provides high PA/US axial resolution. The PA signals is transmitted by a coaxial line connected to the optical-electric rotary joint. The pullback device driven by a stepper motor (PKP546N18B-L, Oriental Motor, Japan) is used to control the pullback of the endoscopic probe. A physical photograph of the 1 mm-diameter endoscopic probe is shown in Fig. 1(c). A photo of the tapered and welded areas of the tapered fiber is shown in Fig. 1(d). The coating must be stripped during the processing of the tapered fibers. The fiber (BD-G25/400-11FA, Nufern, USA) with 25/400 μm (core/cladding diameter) is tapered into fiber with 9/144 μm, and then fused with the fiber (PM-TSF-9/125, Nufern, USA) with the same core diameter. Tapered fibers are manufactured by guangdong provincial key laboratory of photonic functional materials and devices (South China Normal University, Guangzhou, China). The tapered fiber in the system is composed of a Ø25-Ø9 μm tapered fiber and a single-mode fiber with a core diameter of 9 μm. The output end of the tapered fiber is fused with the single-mode fiber through the fiber fusion splicer, so the input end of the tapered fiber is a 25/400 μm (core/cladding diameter) fiber, and the output end is a 9/125 μm single mode fiber. In the actual test, it is found that in the same test environment, the coupling efficiency of 9 μm fiber is 30%, the limit output energy of single pulse is 5 μJ/pulse, and the coupling efficiency of 25/400 μm fiber is 82%, the output energy of single pulse is not less than 13 μJ/pulse. Moreover, due to the influence of numerous devices in the intravascular endoscopic system on laser energy, laser transmission needs to pass through optical-electric rotary joint, optical fiber connector, lens, reflector and so on, which ultimately leads to the significant reduction of the laser energy output of the probe. Figures 1(e) and 1(f) show a laser intensity distribution measured at 2 mm from the probe surface separately using the 25/400 μm fiber and Ø25-Ø9 μm tapered fiber, it is obvious that the laser spot emitted by the probe assembled with the Ø25-Ø9 μm tapered fiber is significantly smaller than emitted by the probe assembled with the 25/400 μm fiber.

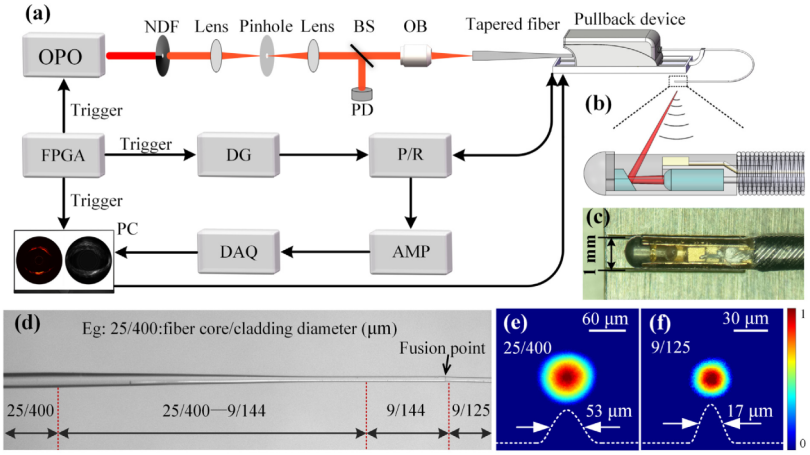

Fig. 1. Schematics of IVPA/US endoscopy with Ø25-Ø9 μm tapered fiber. (a) Schematic of the imaging system. (b) The structure chart of the endoscopic probe. (c) Photograph of the 1 mm-diameter endoscopic probe. (d) Photograph of Ø25-Ø9 μm tapered fiber. (e) Laser-intensity distribution measured at 2 mm from the endoscopic probe surface using 25/400 μm fiber. (f) Laser-intensity distribution measured at 2 mm from the endoscopic probe surface using Ø25-Ø9 μm tapered fiber. OPO, optical parametric oscillator; NDF, neutral density filter; BS, beam splitter; OB, objective; PD, photodiode; DG, delay generator; P/R,

Optics EXPRESS

pulser/receiver; FPGA, field-programmable gate array; AMP, amplifier; DAQ, data-acquisition card.

A field-programmable gate array (FPGA) is employed to trigger the laser, the pulser generator/receiver (5073PR, Olympus, USA), and the high-speed data-acquisition card (M-3i.4120, Spectrum, Germany). The pulser generator/receiver is employed to transmit-80 V amplitude pulses. A delay Generator (DG535, Stanford Research Systems, Sunnyvale, CA, USA) provides timing and delay trigger signals for the laser, acquisition card and US pulse generation, the delay time is 4 μs. The IVPA/US signals were amplified by an amplifier (LNA-650, RFBAY, Gaithersburg, MD, USA). Finally, the 14-bit digitized data-acquisition card with the 250 MS/s sampling rate was used to digitize and record the signal to a personal computer (PC).

3. Results

3.1 Lateral and axial resolution of the IVPA/US system

To verify the lateral and the axial resolutions of the IVPA/US imaging system, PA and US imaging of a carbon fiber with a diameter of 7 μm was performed. Figures 2(a) and 2(e) are PA and US images obtained by the system scanning the carbon fiber at a distance of 2 mm from the probe surface, respectively. Figure 2(b) is an enlarged view of the dotted-line box in Fig. 2(a). Figures 2(c) and 2(d) are the lateral and the axial resolutions of the IVPA system, respectively. The lateral and the axial pixel width were utilized as the line spread functions (LSPs) to evaluate the lateral and the axial resolutions. Based on the LSPs, the lateral resolution of IVPA system is 18 μm, while the axial resolution is 31 μm. Figure 2(f) is an enlarged view of the dotted-line box in Fig. 2(e). Figures 2(g) and 2(h) are the lateral and the axial resolutions of the IVUS, respectively. Based on the LSPs, the lateral resolution of IVUS is 283 μm, while the axial resolution is 31 μm.

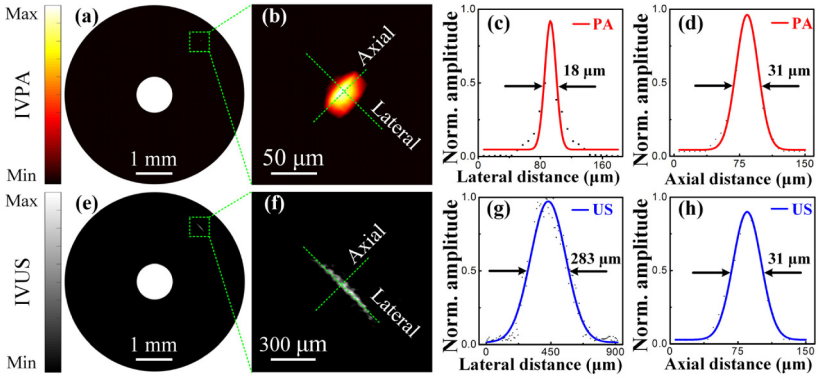

Fig. 2. The lateral and the axial resolutions of IVPA/US system. (a) IVPA B-scan image of a carbon fiber (7 μm in diameter). (b) Enlarged view of dotted-line box in (a). (c) The lateral resolution of IVPA. (d) The axial resolution of IVPA. (e) IVUS B-scan image of a carbon fiber (7 μm in diameter). (f) Enlarged view of the dotted-line box in (e). (g) The lateral resolution of IVUS. (h) The axial resolution of IVUS. IVPA, intravascular photoacoustic; IVUS, intravascular ultrasound.

3.2 PA and US imaging experiments of rabbit abdominal aorta

To demonstrate the imaging performance of the IVPA/US imaging system, a lipid-rich rabbit abdominal aorta with a length (Z) of 19 mm was used for IVPA/US imaging experiments. The rabbit abdominal aorta was fixed in agar and placed in water environment. Three-dimensional (3D) imaging was performed by the 1 mm-diameter endoscopic probe, and the results of the imaging were shown as cross-sectional views of IVPA and IVUS images. 1000 A-lines per cross section were recorded and the PA/US signals were averaged 3 times to

Optics EXPRESS

obtain IVPA and IVUS images. The final output energy of the probe is 1.6 μJ/pulse, corresponding to a laser energy density of 50 mJ/cm^2, which is far below the safety threshold of the ANSI laser safety standard of 1 J/cm^2 [31]. As shown in Figs. 3 (a) - 3(d), the images of the IVPA, IVUS and IVPA/US, and the histological section at Z = 1 mm were shown, respectively. Compared the IVPA image and the histological section, the lipid distribution detected by IVPA corresponds well to that of the histological section. Meantime, the images of the IVPA, IVUS, IVPA/US, and the histological section at Z = 18 mm were shown in Figs. 3 (e) -3(h), respectively. It is worth noting that IVPA imaging at the position of Z = 18 mm not only indicated the lipids in the inner wall of the abdominal aorta, but also disclosed the peri-adventitial adipose (PAA) (the yellow arrows in Figs. 3 (e) and 3(h) point to the peri-adventitial adipose) at 1.8 mm from the intimae. As shown in Fig. 4 (h), the PAA imaged by the IVPA image was confirmed by the corresponding histological section, which demonstrated the deep penetration capability of the IVPA system. Benefit by the high-resolution, deep-penetration imaging performance of the system and high PA axial resolution, the lipid distribution obtained by PA imaging is consistent with stained slices exhibited by the Oil Red O. A radial maximum amplitude projection of the IVPA lipid profile was presented in Fig. 3(i), which visually demonstrated the lipid profile of the abdominal aorta. The lipid areas in IVPA imaging and the histological section were measured and calculated by Image-pro Plus (IPP) software, respectively. The statistic result shows a high correlation between IVPA imaging and histological section shown in Fig. 3(j). The correlation coefficient of the lipid area obtained between the IVPA imaging and histological section is ~0.905 shown in Fig. 3(k), which demonstrates the ability of the IVPA system to accurately image lipid plaques.

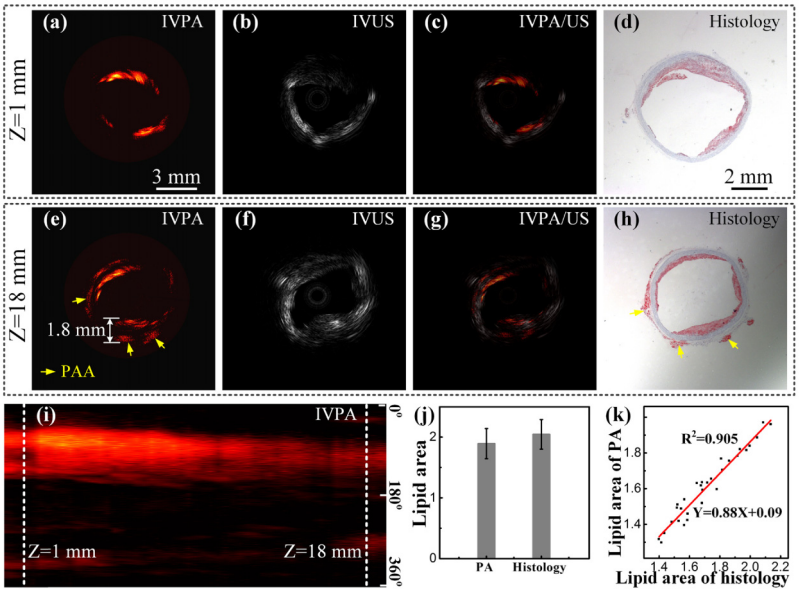

Fig. 3. IVPA/US 2D and 3D images of lipid-rich rabbit abdominal aorta. (a) IVPA image at a position of Z = 1 mm. (b) IVUS image at a position of Z = 1 mm. (c) Overlaid IVPA/IVUS image at a position of Z = 1 mm. (d) Histological photograph at a position of Z = 1 mm. (e) IVPA image at a position of Z = 18 mm. (f) IVUS image at a position of Z = 18 mm. (g) Overlaid IVPA/IVUS image at a position of Z = 18 mm. (h) Histological photograph at a position of Z = 18 mm. (i) Radial maximum projection image based on 3D IVPA data. (j) Mean and mean square deviation error of lipid area in IVPA imaging and histological section. (k) Correlation between IVPA imaging and histological section on the lipid area. PAA, peri-adventitial adipose. (see Visualization 1).

Optics EXPRESS

3.3 PA and US imaging experiments in the blood environment

In order to compare the imaging capabilities of endoscopes assembled with 9 μm fiber (single-mode fiber with core diameter of 9 μm) and endoscope assembled with Ø25-Ø9 μm tapered fiber in the blood environment, the imaging experiments of the lipid-rich rabbit abdominal aorta were carried out in the blood environment. In the experiments, a Pebax material catheter with an inner diameter of 1.2 mm and an outer diameter of 1.3 mm was applied to separate the endoscope probe from the blood environment. To avoid blood clotting, the blood was comprised of 60% fresh rabbit blood, 35% physiological saline, and 5% anticoagulant. The PA/US signals were averaged 5 times to acquire a high-quality IVPA/US image. Figures 4(a) and 4(b) show the IVPA imaging results of an abdominal aorta by the 9 μm fiber-based and the Ø25-Ø9 μm tapered fiber-based endoscopic probes, respectively. Meantime, the corresponding US images and the histological section were shown in Figs. 4(d) and 4(e). By comparing the Oil Red O stained sections, image obtained from the probe with tapered fiber can still display the lipid distribution in the blood environment accurately, while the image obtained from the probe with 9 μm fiber can only display a portion of the lipids. It is worth noting that the IVPA image (Fig. 4(c)) reveals a phenomenon that significant multi- layered of lipids can be observed, which corresponds nicely to histological section of abdominal aorta. The two fitted curves in Figs. 4 (g) and 4(h) (obtained from Figs. 4(c) and 4(f)) show the same characteristics at the same position of the crests and troughs. Four representative regions (I, II, III, and IV) are selected to demonstrate the specific performance of the two curves. The amplitudes of the I, II and IV regions in Figs. 4(g) and 4(h) are higher than that of the III region. Because of a positive correlation between the amplitude of the PA signal and the concentration of the analyte, the lipid concentration in I, II and IV regions are higher than the lipid concentration in III region [32]. The high correlation between the two curves indicates that IVPA imaging can reflect the relative concentration of lipids within the plaque. And the results of related literature indicate that lipid concentration is positively correlated with plaque vulnerability [3]. Therefore, the detection of lipid concentrations provides more parameters for the accurate assessment of atherosclerotic plaque.

Optics EXPRESS

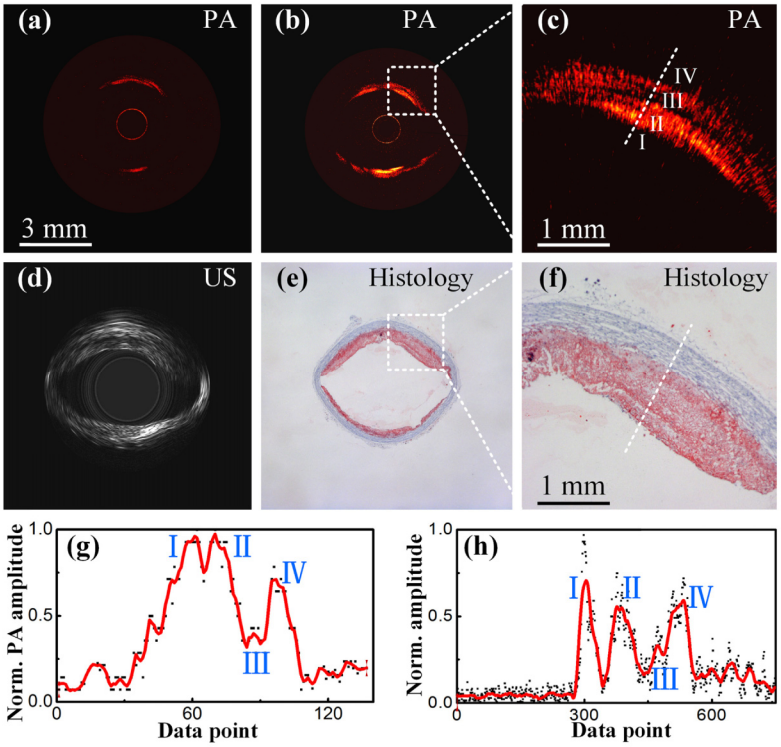

Fig. 4. IVPA/US images of lipid-rich rabbit abdominal aorta in the blood environment and histological graphics. (a) IVPA image by a 9 μm fiber-based endoscopic probe in the blood environment. (b) IVPA image by a Ø25-Ø9 μm tapered fiber-based endoscopic probe in the blood environment. (c) Enlarged view of the dashed box in (b). (d) IVUS imaging. (e) Histological photograph. (f) Enlarged view of the dashed box in (e). (g) A curve fitted to the IVPA data of the dashed line in (c). (h) A curve fitted to the pixel values of the dashed line in (f).

4. Discussion

Although the propagation of laser in a tapered fiber causes partial laser overflow and energy loss (the coupling efficiency of the tapered fiber is 42%), the laser energy output from the tapered fiber is several times higher than that of the single-mode fiber due to the high coupling efficiency of the tapered fiber input end. Therefore, the Ø25-Ø9 μm tapered fiber is a reasonable fiber for IVPA to achieve high-resolution and deep-penetration lipid imaging.

For further research, it is necessary to improve the imaging speed in order to eliminate disadvantageous influences of pulsation artifact, and to achieve IVPA in *vivo* experiments. In this work, the imaging speed of the IVPA imaging system is 0.5 frames per second (FPS), real-time imaging with an imaging speed of 24 FPS will be realized by increasing the repetition frequency of the OPO and reducing the noise to decrease the average number of times in the future. In addition, the application environment of the *in vivo* experiment is pure blood environment, and the influence of blood on the laser spot must be considered. In the future, Monte Carlo simulation will be used to guide the design of the optimal light path to achieve the smallest focused spot in the blood environment, so that the imaging result maintains high-resolution performance.

5. Conclusion

In summary, we developed a Ø25-Ø9 μm tapered fiber-based IVPA/US endoscopy for high-resolution and deep-penetration lipid imaging in the water and the blood. The IVPA

Optics EXPRESS

endoscope obtains the best lateral resolution of 18 μm and a large imaging-depth covered from the intima to the PAA, due to the high coupling efficiency and small output facula of tapered fiber. High-resolution and deep-penetration IVPA images achieved by the IVPA/US endoscope that precisely reflected the lipid distribution and the relative concentration of lipid in the atherosclerotic plaque. Furthermore, a well correlation of the lipid area between PA images and histological staining results has been demonstrated by the biological experiments. These histology-like IVPA images demonstrate the potential of IVPA endoscopy in clinical applications and can be used in the future to more accurate diagnosis of atherosclerotic plaque components.

Funding

National Natural Science Foundation of China (61822505, 61331001, 11774101, 61627827, 81630046, 81571689); The Science and Technology Planning Project of Guangdong Province, China (2015B020233016); The Science and Technology Youth Talent for Special Program of Guangdong, China (2015TQ01X882).

References

1. B. Cannon, "Cardiovascular disease: biochemistry to behaviour," Nature **493**(7434), S2–S3 (2013).
2. L. M. Buja and J. T. Willerson, "Role of inflammation in coronary plaque disruption," Circulation **89**(1), 503–505 (1994).
3. C. V. Felton, D. Crook, M. J. Davies, and M. F. Oliver, "Relation of plaque lipid composition and morphology to the stability of human aortic plaques," Arterioscler. Thromb. Vasc. Biol. **17**(7), 1337–1345 (1997).
4. Y. Cao, J. Hui, A. Kole, P. Wang, Q. Yu, W. Chen, M. Sturek, and J. X. Cheng, "High-sensitivity intravascular photoacoustic imaging of lipid-laden plaque with a collinear catheter design," Sci. Rep. **6**(1), 25236 (2016).
5. W. Wei, X. Li, Q. Zhou, K. K. Shung, and Z. Chen, "Integrated ultrasound and photoacoustic probe for co-registered intravascular imaging," J. Biomed. Opt. **16**(10), 106001 (2011).
6. M. Wu, G. Springeling, M. Lovrak, F. Mastik, S. Iskander-Rizk, T. Wang, H. M. van Beusekom, A. F. van der Steen, and G. Van Soest, "Real-time volumetric lipid imaging in vivo by intravascular photoacoustics at 20 frames per second," Biomed. Opt. Express **8**(2), 943–953 (2017).
7. P. Beard, "Biomedical photoacoustic imaging," Interface Focus **1**(4), 602–631 (2011).
8. C. Li and L. V. Wang, "Photoacoustic tomography and sensing in biomedicine," Phys. Med. Biol. **54**(19), R59–R97 (2009).
9. J. Zhang, S. Yang, X. Ji, Q. Zhou, and D. Xing, "Characterization of lipid-rich aortic plaques by intravascular photoacoustic tomography: ex vivo and in vivo validation in a rabbit atherosclerosis model with histologic correlation," J. Am. Coll. Cardiol. **64**(4), 385–390 (2014).
10. P. Wang, T. Ma, M. N. Slipchenko, S. Liang, J. Hui, K. K. Shung, S. Roy, M. Sturek, Q. Zhou, Z. Chen, and J. X. Cheng, "High-speed intravascular photoacoustic imaging of lipid-laden atherosclerotic plaque enabled by a 2-kHz barium nitrite raman laser," Sci. Rep. **4**(1), 6889 (2015).
11. C. Li, A. Aguirre, J. Gamelin, A. Maurudis, Q. Zhu, and L. V. Wang, "Real-time photoacoustic tomography of cortical hemodynamics in small animals," J. Biomed. Opt. **15**(1), 010509 (2010).
12. D. Cai, G. Li, D. Xia, Z. Li, Z. Guo, and S. L. Chen, "Synthetic aperture focusing technique for photoacoustic endoscopy," Opt. Express **25**(17), 20162–20171 (2017).
13. H. Guo, C. Song, H. Xie, and L. Xi, "Photoacoustic endomicroscopy based on a MEMS scanning mirror," Opt. Lett. **42**(22), 4615–4618 (2017).
14. K. Xiong, S. Yang, X. Li, and D. Xing, "Autofocusing optical-resolution photoacoustic endoscopy," Opt. Lett. **43**(8), 1846–1849 (2018).
15. M. X. Mingjun Xu, P. L. Peng Lei, J. F. Jianqin Feng, F. L. Fangfang Liu, S. Y. Sihua Yang, and P. Z. Pengfei Zhang, "Photoacoustic characteristics of lipid-rich plaques under ultra-low temperature and formaldehyde treatment," Chin. Opt. Lett. **16**(3), 031702 (2018).
16. K. Jansen, A. F. van der Steen, H. M. van Beusekom, J. W. Oosterhuis, and G. van Soest, "Intravascular photoacoustic imaging of human coronary atherosclerosis," Opt. Lett. **36**(5), 597–599 (2011).
17. B. Wang, J. L. Su, J. Amirian, S. H. Litovsky, R. Smalling, and S. Emelianov, "Detection of lipid in atherosclerotic vessels using ultrasound-guided spectroscopic intravascular photoacoustic imaging," Opt. Express **18**(5), 4889–4897 (2010).
18. X. Ji, K. Xiong, S. Yang, and D. Xing, "Intravascular confocal photoacoustic endoscope with dual-element ultrasonic transducer," Opt. Express **23**(7), 9130–9136 (2015).
19. A. B. Karpiouk, B. Wang, J. Amirian, R. W. Smalling, and S. Y. Emelianov, "Feasibility of in vivo intravascular photoacoustic imaging using integrated ultrasound and photoacoustic imaging catheter," J. Biomed. Opt. **17**(9), 0960081 (2012).
20. T. J. Allen, A. Hall, A. P. Dhillon, J. S. Owen, and P. C. Beard, "Spectroscopic photoacoustic imaging of lipid-rich plaques in the human aorta in the 740 to 1400 nm wavelength range," J. Biomed. Opt. **17**(6), 061209 (2012).

Optics EXPRESS

21. X. Bai, X. Gong, W. Hau, R. Lin, J. Zheng, C. Liu, C. Zeng, X. Zou, H. Zheng, and L. Song, "Intravascular optical-resolution photoacoustic tomography with a 1.1 mm diameter catheter," PLoS One **9**(3), 92463 (2014).
22. J. Cai, T. S. Hatsukami, M. S. Ferguson, W. S. Kerwin, T. Saam, B. Chu, N. Takaya, N. L. Polissar, and C. Yuan, "In vivo quantitative measurement of intact fibrous cap and lipid-rich necrotic core size in atherosclerotic carotid plaque: comparison of high-resolution, contrast-enhanced magnetic resonance imaging and histology," Circulation **112**(22), 3437–3444 (2005).
23. Y. Li, X. Gong, C. Liu, R. Lin, W. Hau, X. Bai, and L. Song, "High-speed intravascular spectroscopic photoacoustic imaging at 1000 A-lines per second with a 0.9-mm diameter catheter," J. Biomed. Opt. **20**(6), 065006 (2015).
24. P. Wang, H. W. Wang, M. Sturek, and J. X. Cheng, "Bond-selective imaging of deep tissue through the optical window between 1600 and 1850 nm," J. Biophotonics **5**(1), 25–32 (2012).
25. J. Hui, Q. Yu, T. Ma, P. Wang, Y. Cao, R. S. Bruning, Y. Qu, Z. Chen, Q. Zhou, M. Sturek, J. X. Cheng, and W. Chen, "High-speed intravascular photoacoustic imaging at 1.7 μm with a KTP-based OPO," Biomed. Opt. Express **6**(11), 4557–4566 (2015).
26. M. H. Xu and L. V. Wang, "Photoacoustic imaging in biomedicine," Rev. Sci. Instrum. **77**(4), 041101 (2006).
27. Y. Cao, A. Kole, J. Hui, Y. Zhang, J. Mai, M. Alloosh, M. Sturek, and J. X. Cheng, "Fast assessment of lipid content in arteries in vivo by intravascular photoacoustic tomography," Sci. Rep. **8**(1), 2400 (2018).
28. B. Wang, A. Karpiouk, D. Yeager, J. Amirian, S. Litovsky, R. Smalling, and S. Emelianov, "Intravascular photoacoustic imaging of lipid in atherosclerotic plaques in the presence of luminal blood," Opt. Lett. **37**(7), 1244–1246 (2012).
29. M. Koshiba, K. Saitoh, K. Takenaga, and S. Matsuo, "Multi-core fiber design and analysis: coupled-mode theory and coupled-power theory," Opt. Express **19**(26), B102–B111 (2011).
30. P. K. Upputuri, M. Krisnan, and M. Pramanik, "Microsphere enabled subdiffraction-limited optical-resolution photoacoustic microscopy: a simulation study," J. Biomed. Opt. **22**(4), 045001 (2016).
31. Laser Institute of America, American National Standard for Safe Use of Lasers ANSI Z136.1–2014 (American National Standards Institute, Inc. 2014).
32. H. G. Ma, Z. W. Cheng, Z. Y. Wang, Y. Gu, T. W. Zhang, H. X. Qiu, and S. H. Yang, "Fast linear confocal scanning photoacoustic dermoscopy for non-invasive assessment of chromatodermatosis," Appl. Phys. Lett. **113**(8), 083704 (2018).